3D NUMERICAL SIMULATION OF BASIN EFFECTS ON THE CHARACTERISTICS OF BASIN-TRANSDUCED RAYLEIGH WAVES

J. P. Narayan and Kamal
Department of Earthquake Engineering,
Indian Institute of Technology Roorkee, Roorkee -247 667, INDIA
jaypnfeq@iitr.ernet.in

SUMMARY:
This paper presents the effects of impedance contrast at basin-edge and basin-width on the spectral amplification and complex mode transformation of basin transduced Rayleigh (BTR) waves. BTR-wave, the acronym for basin transduced Rayleigh wave is used in the manuscript. 3D seismic responses of a 2D basin with varying width were computed using a developed 3D fourth-order spatial accurate time-domain finite-difference (FD) algorithm based on parsimonious staggered-grid approximation of 3D viscoelastodynamic wave equations. Analysis of computed seismic responses on the horizontal array across the basin revealed that a complex mode transformation of Rayleigh wave at the basin-edge has caused diffracted body waves, reflected Rayleigh wave and different modes of BTR-waves. Very large amplification of BTR-wave as compared to body waves is obtained for a certain frequency depending on the width of basin. It is concluded that spatial spectral amplification of BTR-wave in basin very much depends on position as well as width of basin. Currently, only body wave amplification in basin is being considered in earthquake resistant designs and seismic microzonation, although surface waves are more damaging as compared to the body waves. Further, the study on amplification of basin-transduced surface waves is very limited. The findings of this paper reveal that basin-edge effects on basin-transduced surface waves deserve a particular attention for the purpose of earthquake resistant designs and seismic microzonation.

Keyword: Characteristics of basin transduced surface wave, spectral amplification of surface waves, 3D finite-difference simulations

1. INTRODUCTION

The seismic motion that takes place at a certain site depends on three factors namely the rupture characteristics of the fault, the travelled path and the local geology. Under favorable circumstances local site effects may largely affect the ground motion characteristics. Significant differences in structural damage in basin as compared with the surrounding exposed rocks or even in the basin itself from place to place have been observed during the earthquakes. A lot of studies have been carried out in the past to quantify the effects of basin resonance and impedance contrast (IC) across the basement on the spectral amplification of body waves in the basins. But, very limited study has been done to quantify the effects of IC across the basin-edge on the spectral amplification and complex mode transformation of basin-transduced surface waves. Although, surface waves are more damaging as compared to the body waves. Rayleigh waves with high frequency content are generated during an earthquake when focal depth is shallow (Narayan and Kumar, 2010). If, these Rayleigh waves enter into a basin, a part of their energy is reflected back and rest is transmitted into the basin. Kawase (1993, 2002) called these types of surface waves inside the basin as 'basin-transduced surface wave'. In basin, near the edge, complex transformation from one mode of surface wave from the surrounding rock to different modes in the basin sediments i.e., mode conversion between two different media, takes place. The existence of basin-transduced surface wave was reported by Hanks (1975), who showed a series of wavelets recorded during San Fernando, California earthquake (1971). The duration of displacement records were short in rocky region and it was quite long and dispersed in the Los Angeles basin. Vidale and Helmberger (1988) simulated low frequency basin-transduced surface

waves in the San Fernando and Los Angeles basin successfully. Sato et al. (1999) reproduced results of the displacement records observed at Tokyo during the Kanto earthquake of 1923 and confirmed the recording of basin-transduced surface wave based on 3D finite difference simulations.

Narayan (2010, 2012) simulated the response of a 2D open basin towards the other basin-edge using P-SV FD algorithmand studied the spectral amplification of BTR-waves at a particular distance from the first basin-edge. He reported that frequency corresponding to the largest spectral amplification of BTR-waves very much depends on the fundamental frequency (F_0) of soil in the basin. An increase of spectral amplification of BTR-waves with increase of IC at the basin edge was also inferred. One of the major draw backs of FD algorithm used by Narayan (2010, 2012) was that damping was not frequency dependent. In this paper, development of a (2, 4) 3D time-domain finite-difference algorithm based on parsimonious staggered grid approximation of viscoelastic wave equation is documented (Emmerich and Korn, 1987; Kristek and Moczo, 2003; Liu and Archuleta, 2006). The developed algorithm has been used to simulate the response of basin having different width on a horizontal array. Spectral amplification of BTR-wave in basin at different locations is analysed in details. VGR-stress imaging technique is implemented on the free surface (Narayan and Kumar, 2008). In order to avoid the edge reflections both the Clayton and Engquist (1977) and Israeli and Orszag (1981) absorbing boundary condition is implemented on the model edges.

2. VISCOELASTIC 3D WAVE EQUATION

Earth's materials remember their past, that is, stress strain relation also depends on time. This is due to the fact that the behavior of the material is combined behavior of both, elastic solids and viscous fluids. Such behavior can be approximated using viscoelastic models of medium. Models witch quite well approximate rheological properties and behavior of the real earth's material can be constructed by connecting the simplest rheological elements, Hooke and Stokes in parallel or series. To incorporate the realistic damping in time domain FD computation, Day and Minster (1984) used the Pade´ approximation to expand a frequency-dependent viscoelastic modulus into an nth-order rational function in order to replace the convolutory integral by n first-order differential equations. Emmerich and Korn (1987) improved the approach by considering the rheology of the generalized Maxwell body (GMB) whose viscoelastic modulus has the desired rational form. Kristek and Moczo (2003) addressed the basic theoretical and algorithmic aspects of memory efficient implementation of realistic attenuation in the staggered grid modeling in media with material discontinuities. Liu and Archuleta (2006) developed an approach to determine the relaxation time and weight coefficients of the relaxation functions based on arithmetic averaging of the viscoelastic moduli.

The viscoelastic wave equation for 3D heterogeneous medium based on anelastic coefficients and anelastic functions can be written as given below (Kristek and Moczo, 2003; Moczo and Kristek, 2005).

$$\rho \frac{\partial^2 U}{\partial t^2} = \frac{\partial \sigma_{xx}}{\partial x} + \frac{\partial \sigma_{xy}}{\partial y} + \frac{\partial \sigma_{xz}}{\partial z} \tag{1}$$

$$\rho \frac{\partial^2 V}{\partial t^2} = \frac{\partial \sigma_{xy}}{\partial x} + \frac{\partial \sigma_{yy}}{\partial y} + \frac{\partial \sigma_{yz}}{\partial z} \tag{2}$$

$$\rho \frac{\partial^2 W}{\partial t^2} = \frac{\partial \sigma_{xz}}{\partial x} + \frac{\partial \sigma_{yz}}{\partial y} + \frac{\partial \sigma_{zz}}{\partial z} \tag{3}$$

$$\sigma_{xx} = \bar{K}_u \left(\frac{\partial U}{\partial x} \right) + \bar{\lambda}_u \left(\frac{\partial V}{\partial y} + \frac{\partial W}{\partial z} \right) - \sum_{l=1}^{m} [\bar{Y}_l^\alpha (\chi_l^{xx}) + \bar{Y}_l^\lambda (\chi_l^{yy} + \chi_l^{zz})] \qquad l = 1, 2, \ldots, m \tag{4}$$

$$\sigma_{yy} = \bar{K}_u \left(\frac{\partial V}{\partial y} \right) + \bar{\lambda}_u \left(\frac{\partial U}{\partial x} + \frac{\partial W}{\partial z} \right) - \sum_{l=1}^{m} [\bar{Y}_l^\alpha (\chi_l^{yy}) + \bar{Y}_l^\lambda (\chi_l^{xx} + \chi_l^{zz})] \qquad l = 1, 2, \ldots, m \tag{5}$$

$$\sigma_{zz} = \bar{K}_u \left(\frac{\partial W}{\partial z}\right) + \bar{\lambda}_u \left(\frac{\partial U}{\partial x} + \frac{\partial V}{\partial y}\right) - \sum_{l=1}^{m} [\bar{Y}_l^\alpha(\chi_l^{zz}) + \bar{Y}_l^\lambda(\chi_l^{xx} + \chi_l^{yy})] \qquad l = 1, 2, \dots, m \quad (6)$$

$$\sigma_{xz} = \bar{\mu}_u \left[\left(\frac{\partial U}{\partial z}\right) + \left(\frac{\partial W}{\partial x}\right)\right] - \sum_{l=1}^{m} [\bar{Y}_l^\beta(\chi_l^{xz})] \qquad l = 1, 2, \dots, m \quad (7)$$

$$\sigma_{xy} = \bar{\mu}_u \left[\left(\frac{\partial U}{\partial y}\right) + \left(\frac{\partial V}{\partial x}\right)\right] - \sum_{l=1}^{m} [\bar{Y}_l^\beta(\chi_l^{xy})] \qquad l = 1, 2, \dots, m \quad (8)$$

$$\sigma_{yz} = \bar{\mu}_u \left[\left(\frac{\partial V}{\partial z}\right) + \left(\frac{\partial W}{\partial y}\right)\right] - \sum_{l=1}^{m} [\bar{Y}_l^\beta(\chi_l^{yz})] \qquad l = 1, 2, \dots, m \quad (9)$$

Where $\bar{K}_u$, $\bar{\lambda}_u$ and $\bar{\mu}_u$ are modified elastic parameters and $\bar{Y}_l^\alpha$, $\bar{Y}_l^\lambda$ and $\bar{Y}_l^\beta$ are the modified anelatic coefficients. $\chi_l^{xx}, \chi_l^{yy}, \chi_l^{zz}, \chi_l^{xy}, \chi_l^{xz}$ and χ_l^{yz} are anelastic functions for normal and shear components. $\frac{\partial}{\partial x}, \frac{\partial}{\partial y}, \frac{\partial}{\partial z}$ and $\frac{\partial}{\partial t}$ are the differential operators. 'm' is the number of relaxation frequency used.
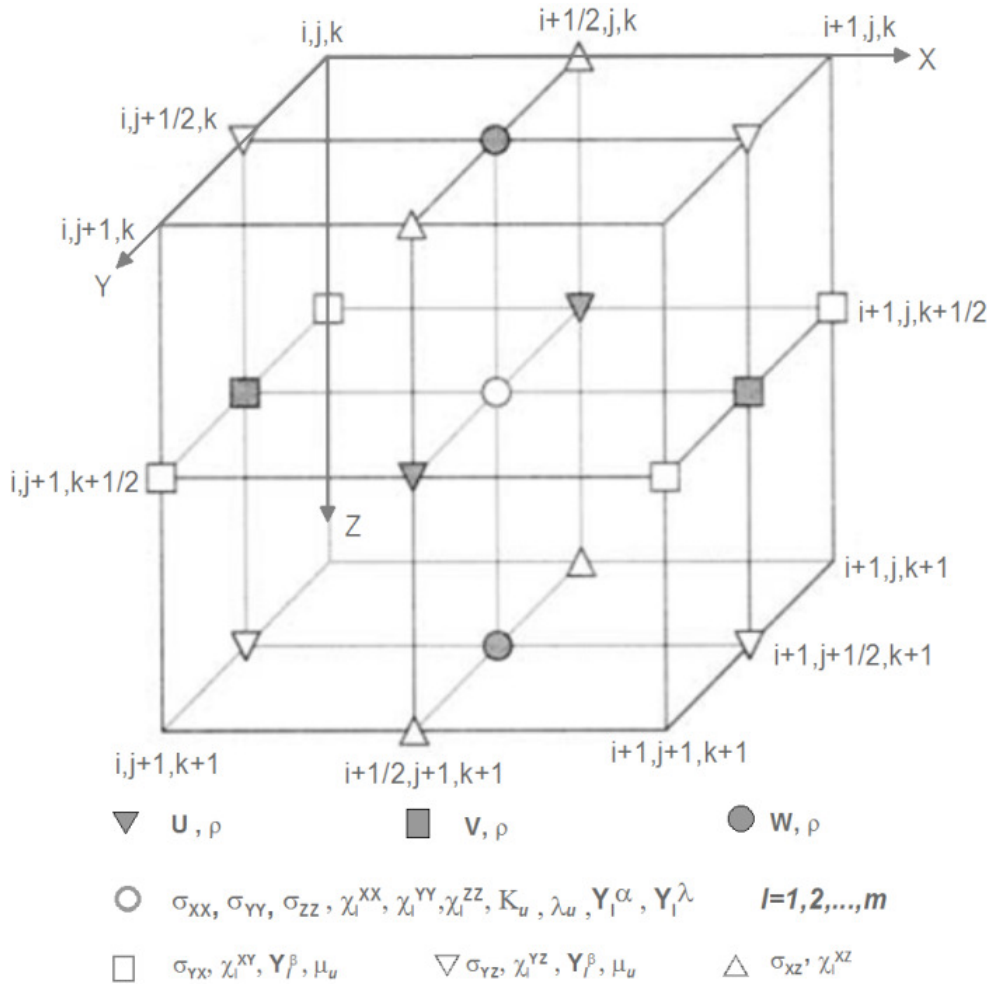

Figure 1. Shows the staggering technique for 3D viscoelastic wave modeling.

Figure 1 shows the staggering technique, where normal stress components σ_{xx}, σ_{yy} and σ_{zz}, unrelaxed elastic parameters K_u and λ_u, anelastic coefficients Y^α and Y^λ and anelastic functions χ^{xx}, χ^{yy} and χ^{zz} are defined at the center of the grid. The particle displacement components U, V and W in the x, y and z-direction and density ρ are defined at the centre of face as shown in figure 1. The shear stresses σ_{xy}, σ_{xz}, σ_{yz}, unrelaxed modulus of rigidity μ_u, anelastic coefficient Y^β and anelastic function χ^{xy}, χ^{xz}, χ^{yz} are defined at the positions as shown in figure 1. λ_u is the unrelaxed Lame's parameter and K_u is equal to sum of λ_u and twice of μ_u.

The material independent anelastic functions χ_l^{xx}, χ_l^{yy}, χ_l^{zz}, χ_l^{xy}, χ_l^{xz} and χ_l^{yz} are given by the following equations. Superscript 'n' denote the time index.

$$(\chi_l^{xx})^{n+1} = \frac{2 - \Delta t \omega_l}{2 + \Delta t \omega_l}(\chi_l^{xx})^n + \frac{2\Delta t \omega_l}{2 + \Delta t \omega_l}\frac{\partial U}{\partial x} \qquad l = 1,2,\dots,m \qquad (10)$$

$$(\chi_l^{yy})^{n+1} = \frac{2 - \Delta t \omega_l}{2 + \Delta t \omega_l}(\chi_l^{yy})^n + \frac{2\Delta t \omega_l}{2 + \Delta t \omega_l}\frac{\partial V}{\partial y} \qquad l = 1,2,\dots,m \qquad (11)$$

$$(\chi_l^{zz})^{n+1} = \frac{2 - \Delta t \omega_l}{2 + \Delta t \omega_l}(\chi_l^{zz})^n + \frac{2\Delta t \omega_l}{2 + \Delta t \omega_l}\frac{\partial W}{\partial z} \qquad l = 1,2,\dots,m \qquad (12)$$

$$(\chi_l^{xy})^{n+1} = \frac{2 - \Delta t \omega_l}{2 + \Delta t \omega_l}(\chi_l^{xy})^n + \frac{2\Delta t \omega_l}{2 + \Delta t \omega_l}\left[\frac{1}{2}\left(\frac{\partial U}{\partial y} + \frac{\partial V}{\partial x}\right)\right] \qquad l = 1,2,\dots,m \qquad (13)$$

$$(\chi_l^{xz})^{n+1} = \frac{2 - \Delta t \omega_l}{2 + \Delta t \omega_l}(\chi_l^{xz})^n + \frac{2\Delta t \omega_l}{2 + \Delta t \omega_l}\left[\frac{1}{2}\left(\frac{\partial U}{\partial z} + \frac{\partial W}{\partial x}\right)\right] \qquad l = 1,2,\dots,m \qquad (14)$$

$$(\chi_l^{yz})^{n+1} = \frac{2 - \Delta t \omega_l}{2 + \Delta t \omega_l}(\chi_l^{yz})^n + \frac{2\Delta t \omega_l}{2 + \Delta t \omega_l}\left[\frac{1}{2}\left(\frac{\partial V}{\partial z} + \frac{\partial W}{\partial y}\right)\right] \qquad l = 1,2,\dots,m \qquad (15)$$

In order to compute the input parameters namely unrelaxed modulus and anelastic coefficients to the FD numerical grid, phase velocity and quality factor at reference frequency (ω_r) is used. The P-wave anelastic coefficients $Y_l^\alpha, l = 1, 2, \dots, m$ and S-wave anelastic coefficients Y_l^β, $l = 1, 2, \dots, m$ have been computed with the help of Futterman's equation (Futterman, 1962) and least square technique for optimization (Kristek and Moczo, 2003).

The modified elastic parameters $\bar{K}_u$, $\bar{\mu}_u$ and $\bar{\lambda}_u$ are computed using the following relationships.

$$\bar{K}_u = K_u\left[1 + \sum_{l=1}^{n} G_{1l}Y_l^\alpha\right] \qquad l = 1,2,\dots,m$$

$$\bar{\mu}_u = \mu_u\left[1 + \sum_{l=1}^{n} G_{1l}Y_l^\beta\right] \qquad l = 1,2,\dots,m \qquad (16)$$

$$\bar{\lambda}_u = \lambda_u\left[1 + \sum_{l=1}^{n} G_{1l}Y_l^\lambda\right] \qquad l = 1,2,\dots,m$$

Similarly, the modified anelastic parameters $\bar{Y}_l^\alpha$, $\bar{Y}_l^\beta$ and $\bar{Y}_l^\lambda$ are computed using the following relationships.

$$\bar{Y}_l^\alpha = G_{2l}K_u Y_l^\alpha \qquad l = 1,2,\dots,m$$

$$\bar{Y}_l^\beta = 2G_{2l}\mu_u Y_l^\beta \qquad l = 1,2,\dots,m \qquad (17)$$

$$\bar{Y}_l^\lambda = G_{2l}\lambda_u Y_l^\lambda \qquad l = 1,2,\dots,m$$

The constants G_{1l} and G_{2l} along with ω as the attenuating angular frequency are given by.

$$G_{1l} = \frac{\Delta t \omega_l}{2 - \Delta t \omega_l} \qquad \text{and} \qquad G_{2l} = \frac{2}{2 - \Delta t \omega_l} \qquad l = 1,2,\dots,m \qquad (18)$$

3. FD APPROXIMATION OF WAVE EQUATION

In equations (1) - (9), the time derivatives were replaced by second order accurate central difference FD operator and space derivatives were replaced by a fourth order staggered grid FD operator (Levander, 1988; Moczo et al., 2000; Narayan and Kumar, 2008). FD approximation of only single component of particle displacement stress component is given in the following equations purposely.

$$
\begin{aligned}
U_{i,j+\frac{1}{2},k+\frac{1}{2}}^{n+1} = {}& 2U_{i,j+\frac{1}{2},k+\frac{1}{2}}^{n} - U_{i,j+\frac{1}{2},k+\frac{1}{2}}^{n-1} + \frac{2\Delta t^2}{\rho_{i,j+\frac{1}{2},k+\frac{1}{2}}(\Delta X_{i-1,j,k} + \Delta X_{i,j,k})} \\
& \left[a\left\{ (\sigma_{xx})_{i+\frac{1}{2},j+\frac{1}{2},k+\frac{1}{2}}^{n} - (\sigma_{xx})_{i-\frac{1}{2},j+\frac{1}{2},k+\frac{1}{2}}^{n} \right\} + b\left\{ (\sigma_{xx})_{i+\frac{3}{2},j+\frac{1}{2},k+\frac{1}{2}}^{n} - (\sigma_{xx})_{i-\frac{3}{2},j+\frac{1}{2},k+\frac{1}{2}}^{n} \right\} \right] + \\
& \frac{\Delta t^2}{\rho_{i,j+\frac{1}{2},k+\frac{1}{2}}\Delta Y_{i,j,k}} \left[a\left\{ (\sigma_{xy})_{i,j+1,k+\frac{1}{2}}^{n} - (\sigma_{xy})_{i,j,k+\frac{1}{2}}^{n} \right\} + b\left\{ (\sigma_{xy})_{i,j+2,k+\frac{1}{2}}^{n} - (\sigma_{xy})_{i,j-1,k+\frac{1}{2}}^{n} \right\} \right] + \\
& \frac{\Delta t^2}{\rho_{i,j+\frac{1}{2},k+\frac{1}{2}}\Delta Z_{i,j,k}} \left[a\left\{ (\sigma_{xz})_{i,j+\frac{1}{2},k+1}^{n} - (\sigma_{xz})_{i,j+\frac{1}{2},k}^{n} \right\} + b\left\{ (\sigma_{xz})_{i,j+\frac{1}{2},k+2}^{n} - (\sigma_{xz})_{i,j+\frac{1}{2},k-1}^{n} \right\} \right]
\end{aligned}
\tag{19}
$$

$$
\begin{aligned}
(\sigma_{xx})_{i+\frac{1}{2},j+\frac{1}{2},k+\frac{1}{2}}^{n} = {}& \frac{(\overline{K}_u)_{i+\frac{1}{2},j+\frac{1}{2},k+\frac{1}{2}}}{\Delta X_{i,j,k}} \left[a\left\{ U_{i+1,j+\frac{1}{2},k+\frac{1}{2}}^{n+1} - U_{i,j+\frac{1}{2},k+\frac{1}{2}}^{n+1} \right\} \right. \\
& \left. + b\left\{ U_{i+2,j+\frac{1}{2},k+\frac{1}{2}}^{n+1} - U_{i-1,j+\frac{1}{2},k+\frac{1}{2}}^{n+1} \right\} \right] + \\
& \frac{(\overline{\lambda}_u)_{i+\frac{1}{2},j+\frac{1}{2},k+\frac{1}{2}}}{\Delta Y_{i,j,k}} \left[a\left\{ V_{i+\frac{1}{2},j+1,k+\frac{1}{2}}^{n+1} - V_{i+\frac{1}{2},j,k+\frac{1}{2}}^{n+1} \right\} + b\left\{ V_{i+\frac{1}{2},j+2,k+\frac{1}{2}}^{n+1} - V_{i+\frac{1}{2},j-1,k+\frac{1}{2}}^{n+1} \right\} \right] + \\
& \frac{(\overline{\lambda}_u)_{i+\frac{1}{2},j+\frac{1}{2},k+\frac{1}{2}}}{\Delta Z_{i,j,k}} \left[a\left\{ W_{i+\frac{1}{2},j+\frac{1}{2},k+1}^{n+1} - W_{i+\frac{1}{2},j+\frac{1}{2},k}^{n+1} \right\} + b\left\{ W_{i+\frac{1}{2},j+\frac{1}{2},k+2}^{n+1} - W_{i+\frac{1}{2},j+\frac{1}{2},k-1}^{n+1} \right\} \right] \\
& - \left\{ (\overline{Y}_1^\alpha)_{i+\frac{1}{2},j+\frac{1}{2},k+\frac{1}{2}} (\chi_1^{xx})_{i+\frac{1}{2},j+\frac{1}{2},k+\frac{1}{2}}^{n+1} + (\overline{Y}_1^\lambda)_{i+\frac{1}{2},j+\frac{1}{2},k+\frac{1}{2}} \left[(\chi_1^{yy})_{i+\frac{1}{2},j+\frac{1}{2},k+\frac{1}{2}}^{n+1} + (\chi_1^{zz})_{i+\frac{1}{2},j+\frac{1}{2},k+\frac{1}{2}}^{n+1} \right] \right\} \\
& - \left\{ (\overline{Y}_2^\alpha)_{i+\frac{1}{2},j+\frac{1}{2},k+\frac{1}{2}} (\chi_2^{xx})_{i+\frac{1}{2},j+\frac{1}{2},k+\frac{1}{2}}^{n+1} + (\overline{Y}_2^\lambda)_{i+\frac{1}{2},j+\frac{1}{2},k+\frac{1}{2}} \left[(\chi_2^{yy})_{i+\frac{1}{2},j+\frac{1}{2},k+\frac{1}{2}}^{n+1} + (\chi_2^{zz})_{i+\frac{1}{2},j+\frac{1}{2},k+\frac{1}{2}}^{n} \right] \right\} \\
& - \left\{ (\overline{Y}_3^\alpha)_{i+\frac{1}{2},j+\frac{1}{2},k+\frac{1}{2}} (\chi_3^{xx})_{i+\frac{1}{2},j+\frac{1}{2},k+\frac{1}{2}}^{n+1} + (\overline{Y}_3^\lambda)_{i+\frac{1}{2},j+\frac{1}{2},k+\frac{1}{2}} \left[(\chi_3^{yy})_{i+\frac{1}{2},j+\frac{1}{2},k+\frac{1}{2}}^{n+1} + (\chi_3^{zz})_{i+\frac{1}{2},j+\frac{1}{2},k+\frac{1}{2}}^{n} \right] \right\} \\
& - \left\{ (\overline{Y}_4^\alpha)_{i+\frac{1}{2},j+\frac{1}{2},k+\frac{1}{2}} (\chi_4^{xx})_{i+\frac{1}{2},j+\frac{1}{2},k+\frac{1}{2}}^{n+1} + (\overline{Y}_4^\lambda)_{i+\frac{1}{2},j+\frac{1}{2},k+\frac{1}{2}} \left[(\chi_4^{yy})_{i+\frac{1}{2},j+\frac{1}{2},k+\frac{1}{2}}^{n+1} + (\chi_4^{zz})_{i+\frac{1}{2},j+\frac{1}{2},k+\frac{1}{2}}^{n} \right] \right\}
\end{aligned}
\tag{20}
$$

4. SIMULATION OF BTR-WAVES:

In order to study the effects of basin-width on the spectral amplification and complex mode transformation of basin transduced Rayleigh (BTR) waves, seismic responses of basin having width as 100 m, 200 m, 400 m, 800 m and 1200 m were computed. X-axis and Y-axis are pointing towards north and east, respectively. The considered basin with edge slope 90° and soil thickness 120 m was

infinitely extended in east-west direction, as shown in figure 2. The model parameters namely velocities and quality factors at reference frequency, density and unrelaxed moduli for both the sediment in basin and basement are given in Table 1. The centre points of all the basins and the array was 2.1 km north of the epicenter. Seismic responses were computed at 41 equidistant (40 m apart) receiver points extending from 1.3 to 2.9 km north of epicentre. A plane Rayleigh wave front oriented in east-west direction was implemented into numerical grid using a line source at a depth of 70 m using Ricker wavelet as source excitation function with 4.0 Hz dominant frequency. The time step was taken as 0.0008 s. The spectral bandwidth of recorded Rayleigh wave at a distance of 1.86 km north of epicenter are shown in figure 2b. In order to compute the spectral amplification of BTR-waves, seismic responses of model with and without the basins were computed.
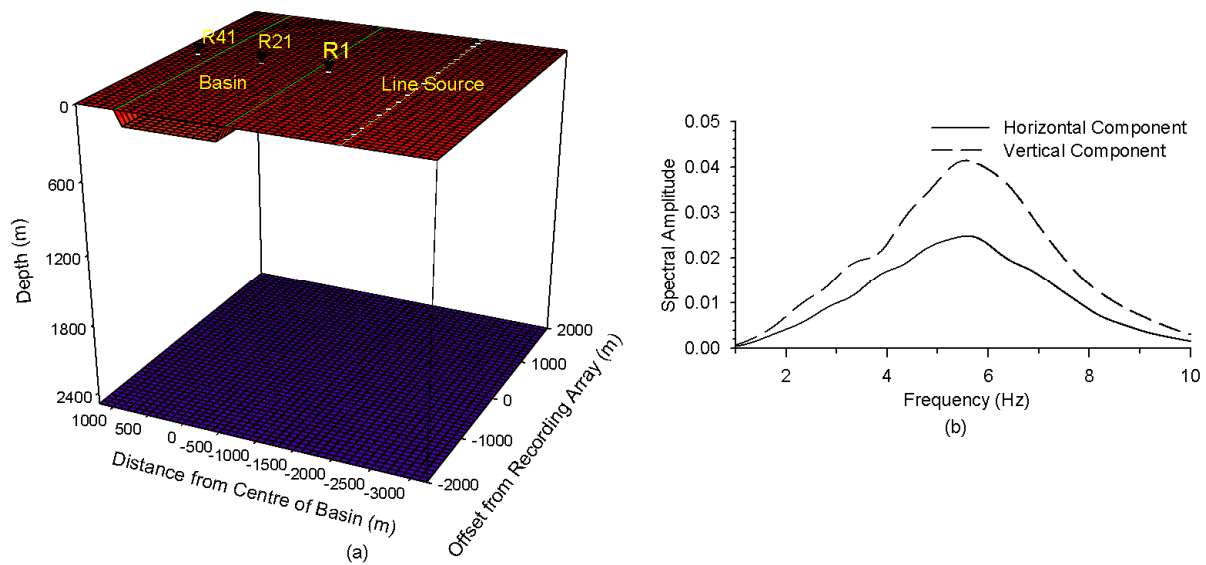

Figure 2a&b. 3D closed basin model and spectral amplitude of Rayleigh wave computed at 1.9 km north of epicenter, respectively.

Table 1. Soil and hard rock parameters considered

Earth Rheology	Parameters at reference frequency (fr)			Density (g/cc)	Poisson ratio (v)	Unrelaxed moduli		
	V_p(m/sec)	V_s(m/sec)	$Q_p=Q_s$			μu (GPA)	$K_u= (\lambda+2\mu)$ (GPA)	λu (GPA)
Soil	1870	1000	100	1.8	0.3	1.853	6.481	2.774
Rock	5542	3200	320	2.8	0.25	28.935	86.788	28.918

Figure 3 depicts the horizontal and vertical components of seismic response of model without considering the basin (means half-space model). The Rayleigh wave amplitude on vertical component is more than that in horizontal component. There is minor decrease of amplitude due anelastic damping only. Figure 4 shows the response of basin with 800 m width. Analysis of this figure depicts complex mode transformation of Rayleigh wave at southern basin-edge. Reflected Rayleigh wave and possible diffracted body waves from the southern basin-edge can be inferred. Further, different modes of BTR-wave can also be inferred. The earlier arrivals of BTR waves are less dispersed and horizontally polarised. On the other hand, the later arrivals of BTR-waves are highly dispersed and vertically polarised. The amplitude of different modes of BTR-wave in basin are highly variable with location. Seismic responses of basin with width as 1200 m are shown in figure 5. Similar observations can be inferred as was in case of basin width 800 m. There is leakage of BTR-wave in rock at each reflection from the north and south basin-edges. There is increase of duration of shaking with the increase of width of basin.
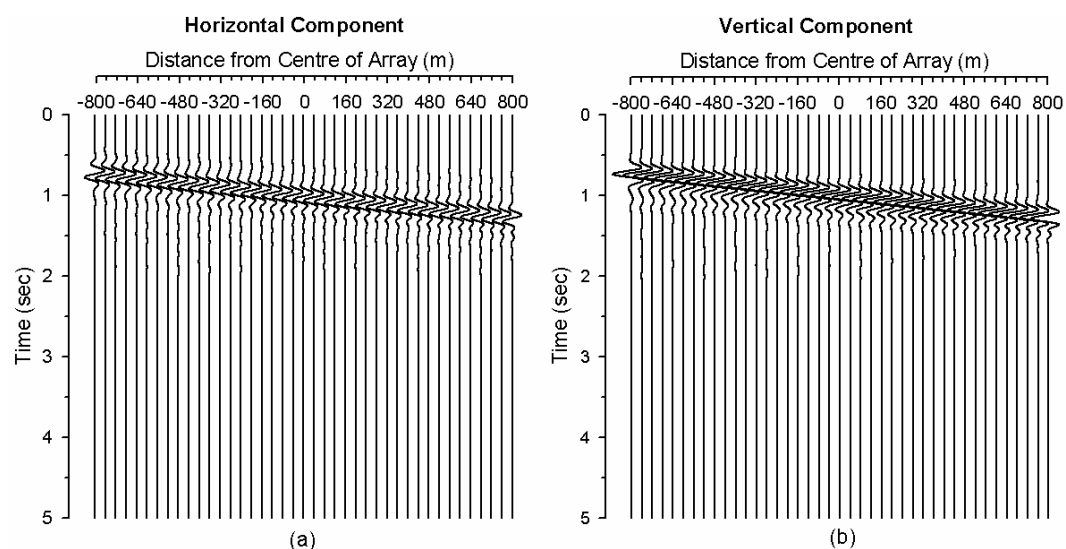
Figure 3a&b. Simulated response of half-space model on a horizontal array.
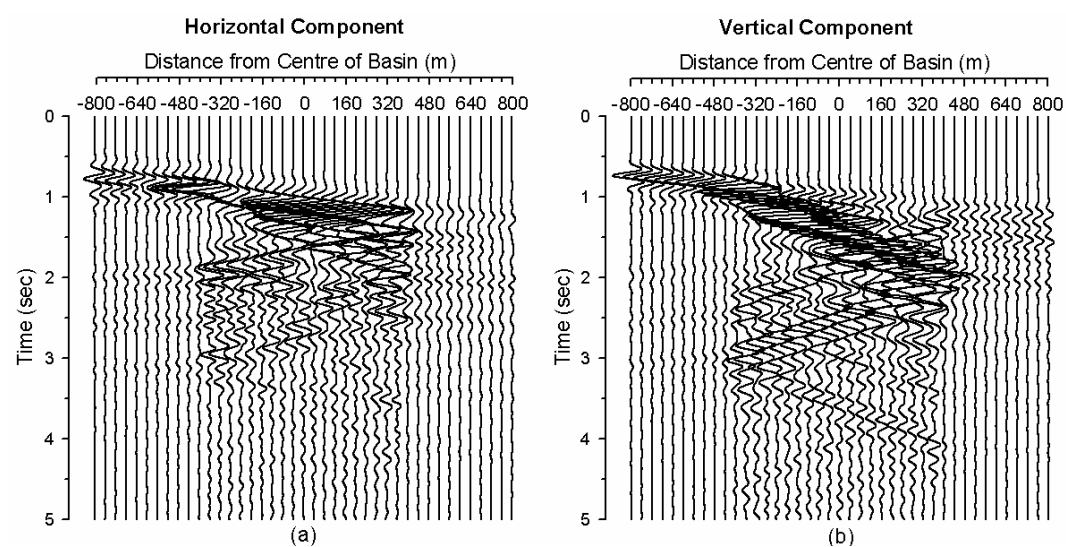

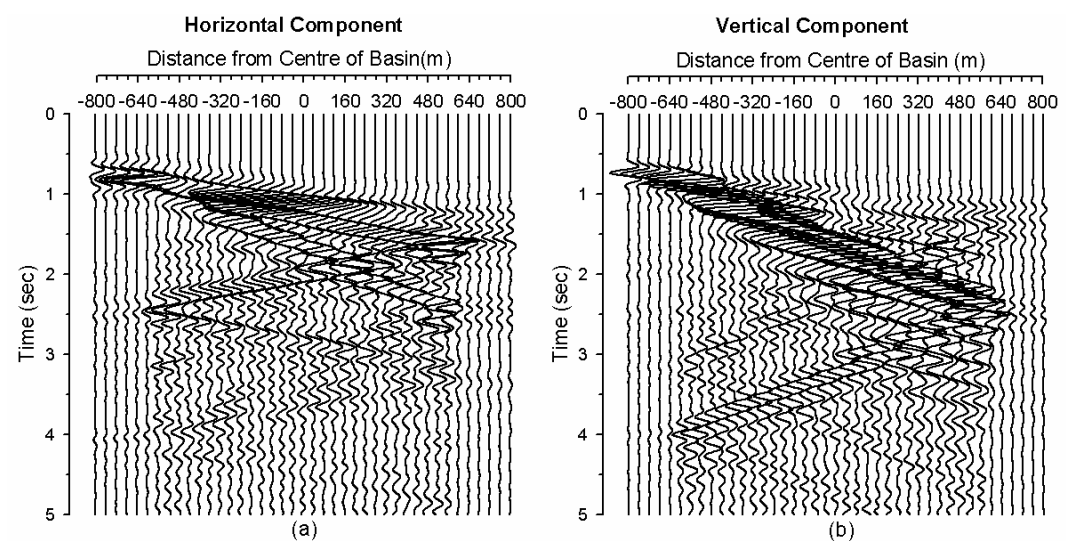**Figure 4a&b.**Seismic response of closed basin of width 800 m.

Figure 5a&b. Seismic response of closed basin of width1200 m.

Figure 6 shows that spectral amplification of both the components of BTR-waves in different basins. On an average spectral amplification of BTR-waves in horizontal components is greater than that in vertical components. The largest spectral amplification of the order of 12 was obtained in horizontal component at the centre of basin of width 200 m. This amplification is larger than sum of P-wave and S-wave ICs. The number of spectral peaks and troughs are increasing with the increase of width of basin, probability due to dispersion effect. In case of larger basin-width spectral amplification seems to be larger in only horizontal component towards north-edge of basin.
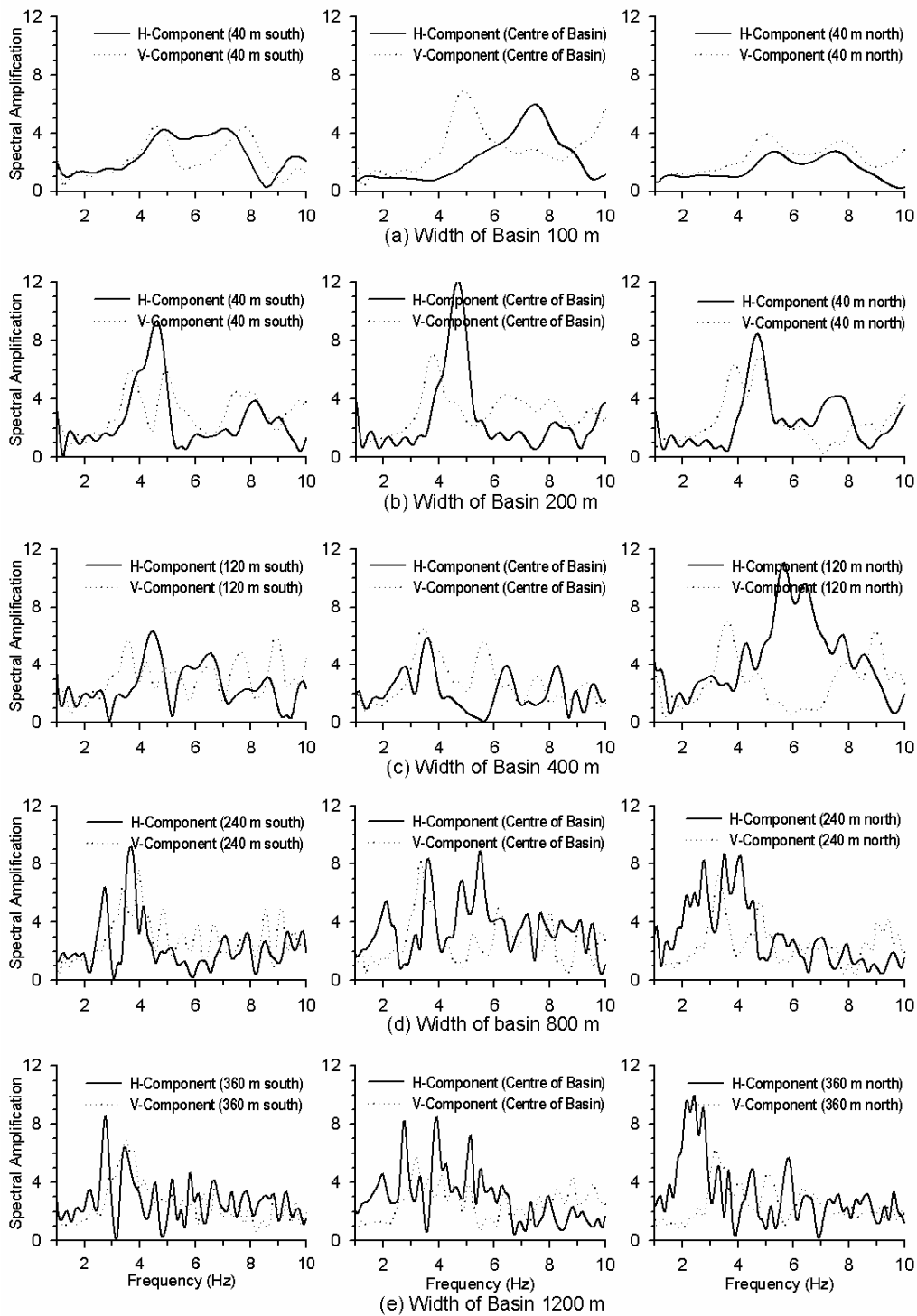

Figure 6. Spectral amplification of Rayleigh wave in different basins.

The spatial variation of average spectral amplification in basins is shown in figure 7. The average spectral amplification was larger in vertical components in case of basins having width less than 200 m. But, reverse was the case when basin-width was more than 200 m. Further, average spectral amplification in horizontal components was larger towards the north basin-edge and reverse is the case in vertical component. There is on an average increase of average spectral amplification from south to north basin-edge in horizontal component and reverse is the case in vertical component.
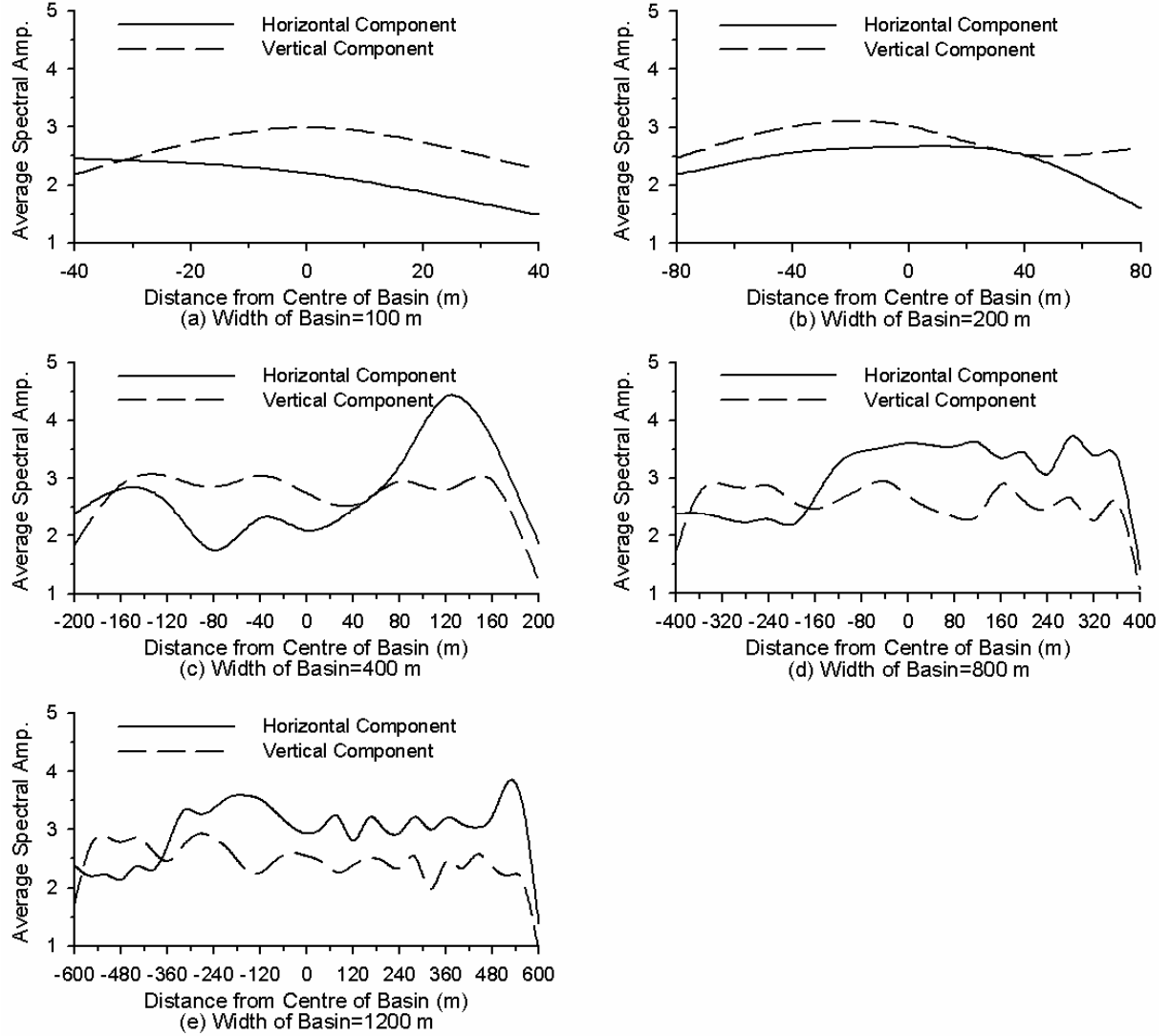

Figure 7. Average spectral amplification of Rayleigh wave.

5. DISCUSSION AND CONCLUSIONS

A new (2, 4) 3D staggered-grid FD algorithm is developed based on the GMB-EK rheological model in order to incorporate the frequency dependent damping in the time domain simulations (Day and Minster, 1984; Emmerich and Korn, 1987; Kristek and Moczo, 2003; Moczo and Kristek, 2005). The analysis of various simulated results revealed a complex mode transformation of Rayleigh waves after entering into the basin (Kawase, 1993, 2002). The less dispersed earlier arrivals of BTR-wave have more amplitude in the horizontal component as compared to the vertical component but reverse was the case for the highly dispersed later arrivals of the BTR-waves. The largest spectral amplification in horizontal component of the order of 12 was more than the twice of the ICs across the basin-edge.

On an average the average spectral amplification in horizontal component was more except when basin-width was less than 200 m. Further, average spectral amplification of horizontal component was increasing towards the northern basin-edge and reverse was the case in vertical component.

ACKNOWLEDGMENTS

REFERENCES

1. Clayton, R.W. and Engquist, B., (1977). Absorbing boundary conditions for acoustic and elastic wave equations. *Bulletin of Seismological Society of America* **67**, 1529-1540.
2. Day, S.M. and Minster, J.B., (1984). Numerical simulation of attenuated wave field using a pade approximant method. *Geophysical Journal of the Royal Astronomical Society* **78**, 105-118.
3. Emmerich, H. and Korn, M., (1987). Incorporation of attenuation into time-domain computations of seismic wavefield. *Geophysics* **52**, 1252-1264.
4. Futterman, W. I., (1962). Dispersive body waves. *Journal of Geophysics Research* **67**, 5279 -5291.
5. Hanks, T. C., (1975). Strong Ground Motion of the San Fernando, California Earthquake: Ground Displacements. *Bulletin of the Seismological Society of America* **65**, 193-225.
6. Israeli, M. and Orszag, S.A., (1981). Approximation of Radiation Boundary Conditions. *Journal of Computational Physics* **41**, 115-135.
7. Kawase, H., (1993). Effects of surface and subsurface irregularities in 'Earthquake and ground motions', Architectural Institute of Japan, part 1, chapter **3**, 118-155.
8. Kawase, H., (2002). Site effects on strong ground motions in 'International Handbook of Earthquake and Engineering Seismology, *Ed. Lee et al.', part B*, chapter **61**, 1013-1030.
9. Kristek, J., Moczo, P., (2003). Seismic wave propagation in viscoelastic media with material discontinuities – a 3D 4th-order staggered-grid finite-difference modeling. *Bulletin of the Seismological Society of America* **93**, 2273-2280.
10. Levander, A.R., (1988). Fourth-order finite-difference P-SV seismograms. *Geophysics* **53**, 1425-1436.
11. Liu, P. and Archuleta, R. J. (2006). Efficient Modeling of Q for 3D Numerical Simulation of Wave Propagation. *Bulletin of the Seismological Society of America* **96**, 1352–1358.
12. Moczo, P., Kristek, J. and Halada, L., (2000). 3D fourth-order staggered grid finite-difference schemes: stability and grid dispersion. *Bulletin of the Seismological Society of America* **90**, 587–603.
13. Moczo, P. and Kristek, J., (2005). On the rheological models used for time-domain methods of seismic wave propagation. *Geophysical Research letters* **32**, L01306, doi:10.1029/2004GL021598.
14. Narayan, J.P. and Kumar, S., (2010). Study of effects of focal depth on the characteristics of Rayleigh waves using finite-difference method. *Acta Geophysica* **58**, 624-644.
15. Narayan, J.P., (2010). Effects of impedance contrast and soil thickness on the basin transduced Rayleigh waves and associated differential ground motion. *Pure and Applied Geophysics* **167**, 1485-1510.
16. Narayan, J.P., (2012). Effects of P-wave and S-wave impedance contrast on the characteristics of basin transduced Rayleigh waves. *Pure and Applied Geophysics* DOI 10.1007/s00024-011-0338-7.
17. Narayan, J.P., and Kumar, S., (2008). A fourth order accurate SH-wave staggered grid finite-difference algorithm variable grid size and VGR-stress imaging technique. *Pure and Applied Geophysics* **165**, 271-295.
18. Sato, T., Graves, R.W. and Somerville, P.G., (1999). 3-D finite difference simulation of long-period strong motions in the Tokyo Metropolitan Area during the 1990 Odawa earthquake (Ms 5.1) and the great 1923 Kanto earthquake (Ms 8.2) in Japan. *Bulletin of the Seismological Society of America* **89**, 579-607.
19. Vidale, J.E. and Helmberger, D.V., (1988). Elastic finite-difference modeling of the 1971 San Fernando, California earthquake. *Bulletin of the Seismological Society of America* **78**, 122-144.